RSC Advances

PAPER

View Article Online
View Journal | View Issue

Cite this: *RSC Adv.*, 2026, **16**, 17219

Low thermal stress and high-strength interface in brazing welding Nd:YAG-based advanced laser components

Baolin Zhang,†[a] Xiaojian Xu,†[b] Guangwei Sun,[a] Cheng Yang,[a] Ge Zhang,[c] Haichao Cui,*[b] Mingjian Wang,*[a] Guofeng Xin,[a] Xia Hou[a] and Weibiao Chen[a]

Cu/Nd:YAG joints present a critical challenge for packaging advanced Nd:YAG-based laser components. Owing to the significant mismatch in the thermal expansion coefficients and the poor metallurgical compatibility between the ceramic and metal, the resulting high thermal stress and serious void defects deteriorate beam quality and structural lifetime. In this work, Cu and Nd:YAG were subjected to braze welding at a lower temperature of 190 °C, with reduced thermal stress and sound. It was obtained by designing a Ti–Pt–Au film as the transition layer and employing a vacuum-deposited indium film as the welding layer. Based on this approach, herein, practical sandwiched Cu/Nd:YAG/Cu laser components were fabricated for space-grade applications. Under extreme service conditions of satellite-borne laser systems, including large diurnal temperature variations and complex cyclic loads, the tested beam morphology and simulated thermal stress of the prepared laser component during operation satisfied the application requirements. These findings not only provide an efficient packaging solution for Nd:YAG-based laser components but also enrich the theoretical foundation for achieving low thermal stress and high-strength interface in ceramic/metal dissimilar joints.

Received 18th October 2025
Accepted 13th February 2026

DOI: 10.1039/d5ra07977b

rsc.li/rsc-advances

1. Introduction

With the rapid progress in laser technology, high-performance Nd:YAG-based solid-state laser components have been widely applied in space-related technologies, including deep-space communication and ranging.[1–3] The crucial step during the integrated packing fabrication of these components lies in joining the Nd:YAG thin-slab crystals and high-thermal-conductivity heat sinks (typically Cu).[4,5] It was mainly achieved by a heterogeneous brazing welding process, in which the voids are usually formed. The voids decrease the heat dissipation area of Cu, hindering efficient heat transfer and promoting higher thermal stress, which induces crystal cracking and beam distortion. Notably, considering the large diurnal temperature variations and complex cyclic loads suffered by satellite-borne laser systems, these voids tend to serve as the initial crack and cause accidents due to structural failure. Therefore, it is essential to achieve both lower thermal stress and high-strength interface during the dissimilar welding of Cu/Nd:YAG for enabling high-performance Nd:YAG-based solid-state laser components in demanding space applications.[6,7]

The brazing welding of Cu and Nd:YAG presents a typical metal/ceramic joining challenge.[8–10] The large difference in the thermal expansion coefficient (CTE) of Cu (16.5×10^{-6} K^{-1}) and Nd:YAG (7.8×10^{-6} K^{-1}) induces significant stress concentration (300–500 MPa) at the dissimilar interface during welding thermal cycling, which significantly weakens the mechanical properties of the joint.[11–13] To address this issue, it is necessary to optimize the brazing parameters, mainly reducing the brazing temperature.[14,15] It serves as the direct but efficient pathway to mitigate thermal stress by reducing heat input while proposing the higher requirement for solder selection and transition layer design.[16]

The traditional Ag–Cu–Ti solder, known for its excellent wettability and bonding strength, has been widely adopted in joining ceramics with metals. However, the melting point of this solder system is relatively high, more than 800 °C, which causes serious thermal damage to temperature-sensitive crystal materials such as Nd:YAG. The large heat input triggers higher stress and microcracks, lowering the component damage threshold.[17] Recently, the low-temperature In-based solder system has received significant attention in the welding process during packaging Nd:YAG-based solid-state laser components. The core advantage of the low-temperature indium-based solder systems lies in their extremely low void fraction and excellent

[a]*Aerospace Laser Technology and System Department, Shanghai Institute of Optics and Fine Mechanics, Chinese Academy of Sciences, Shanghai 201800, PR China. E-mail: haichaocui@sjtu.edu.cn*

[b]*Shanghai Key Laboratory of Materials Laser Processing and Modification, School of Materials Science and Engineering, Shanghai Jiao Tong University, Shanghai 200240, PR China. E-mail: wmjian@siom.ac.cn*

[c]*Precision Optical Manufacturing and Testing Center, Shanghai Institute of Optics and Fine Mechanics, Chinese Academy of Sciences, Shanghai 201815, PR China*

† These authors contributed equally to this work.

ductility, which can effectively solve stress problems in large-sized packaging, especially suitable for laser component packaging with high reliability requirements. Specifically, the high ductility of the indium-based solder accommodates thermally induced deformation without crack initiation, while the minimized void fraction after process optimization ensures stable interfacial contact, resulting in enhanced reliability and reduced thermal resistance of the packaging interface. The In solder is commonly used, together with the Au-coated crystal surface.[18–20] The reaction characteristics of low-temperature chemical combination (~150 °C for Au and In) and high-temperature service (melting points of $AuIn_2$ at ~541 °C and AuIn at ~480 °C) endowed a large potential for preparing space laser components suffering severe diurnal temperature difference. The In solder is usually provided in a commercial $In_{97}Ag_3$ piece but it faced a high interface failure risk. Koo *et al.*[21] considered that compared with Au atoms with slower diffusion rates, the migration of In atoms with faster rates induced vacancy aggregation and formed large-sized Kirkendall pores at the In-side of the dissimilar interface, thereby weakening the interface bond strength and worsening the laser output quality. Xiong *et al.*[22] further found that as the eutectic reaction layer thickened, In atoms may even penetrate into the interior of the crystal substrate, significantly reducing structural reliability. Wen *et al.*[23] found that when the thickness of the reaction layer exceeded the critical value of 2 μm and pore defects significantly worsened, despite moderate reaction-layer growth, which helped improve the bonding strength. Therefore, how to ensure the bonding strength but avoid void formation was crucial for further broadening the In/Au reaction system application in dissimilar welding of Cu/Nd:YAG. Regarding the transition layer design, mainstream methods include two aspects, including placing an additional metal layer and improving the crystal itself, such as modification by ion implanting AuNPs[24] and designing transition layers. The study focuses on the former, a well-designed transition layer should simultaneously achieve the functions including stress regulation, element diffusion barrier and reductable surface modification, but few studies have been conducted in Cu/Nd:YAG dissimilar joints.[25,26]

Herein, low-temperature brazing of Cu/Nd:YAG was successfully achieved at 190 °C. The proposed vacuum-deposited pure In film was compared with a commercial $In_{97}Ag_3$ alloy foil in terms of weld formation and interfacial strength. By employing the deposited In coating as a welding layer and designing a Ti–Pt–Au transition layer, a practical sandwiched Cu/Nd:YAG/Cu space laser component was fabricated. To verify the application feasibility of the process into the extreme service conditions of satellite-borne laser systems, including large diurnal temperature fluctuations and complex cyclic loads, the beam morphology and thermal stress of the prepared laser component were experimentally evaluated and numerically simulated, respectively. This study not only provides an efficient packaging solution for the Nd:YAG-based laser components but also enriches the theoretical foundation for achieving low thermal stress and high-strength interface in other crystal/metal dissimilar joints.

2. Materials and experimental procedure

2.1. Materials and pre-brazing setup

The customized thin-strip Nd:YAG gain medium with a size of 18.0 × 10.0 × 1.8 (mm) was used. Both sides were coated with dual-wavelength anti-reflection films of 1064 nm and 808 nm to optimize beam transmission efficiency. After sealing the vacuum chamber, Ti–Pt–Au metallization layers were deposited on the crystal surface using the magnetron sputtering system (DENTON Discovery-785, USA) under preset process parameters, ensuring that coating performance met subsequent soldering requirements. By coordinating the three layers, a gradient transition in the thermal expansion coefficient at 5×10^{-6} K^{-1} was achieved. Then, the preprocessed Nd:YAG crystal and heat sink were cleaned to remove contaminants and oxides for the subsequent welding process. For solder filling, the dense indium layer was deposited on the crystal surface *via* vacuum thermal evaporation (DENTON, Integrity-22, USA). For the control group, the $In_{97}Ag_3$ alloy foil was employed. To ensure dimensional stability and precise alignment during bonding, a custom-designed metering counterweight was applied to maintain uniform pressure across the bonding surface.

2.2. Brazing welding process

In the initial exploration for an appropriate solder form, a heterogeneous pre-brazing setup was obtained, consisting of a vacuum-deposited pure indium layer on the lower interface and an $In_{97}Ag_3$ alloy foil on the upper (Fig. 1(a)). This process design was based on the thermal conductivity characteristics of the heating plate, resulting in a temperature gradient of approximately 15 °C between the upper and lower brazing interfaces. It was due to the fact that the deposited pure indium solder possessed the melting point of 156.7 °C, while the melting point of the $In_{97}Ag_3$ piece was 143.0 °C. The brazing welding process of the assembled Nd:YAG crystal and heat sink was conducted in a vacuum welding furnace (VACUNITE 180, GE). The pre-defined heating curve was set. The recommended welding condition was 0.1 MPa (1 bar) pressure at 190 °C for 12 minutes. After the welding process, the assembly remained in a vacuum environment for a designated period to release residual stresses and trapped gases.

Furthermore, the vacuum deposited In/vacuum deposited In double-sided brazing process developed in this study adopts an innovative symmetrical indium plating structure design under the same welding conditions (Fig. 1(b)). By adopting the Ti–Pt–Au composite transition layer design and precise control of Au layer thickness and plasma surface activation technology, the bonding rate between the gold plating heat sink and the laser crystal Nd:YAG was significantly improved. The Nd:YAG crystal (wavelength 1064 nm) treated with metallization forms a "sandwich" structure with a gold-plated heat sink. This assembly process achieves efficient soldering at low temperatures (below 200 °C) through a Ti–Pt–Au transition layer, meeting the high reliability requirements of space-level lasers for component packaging. This technology breaks through the

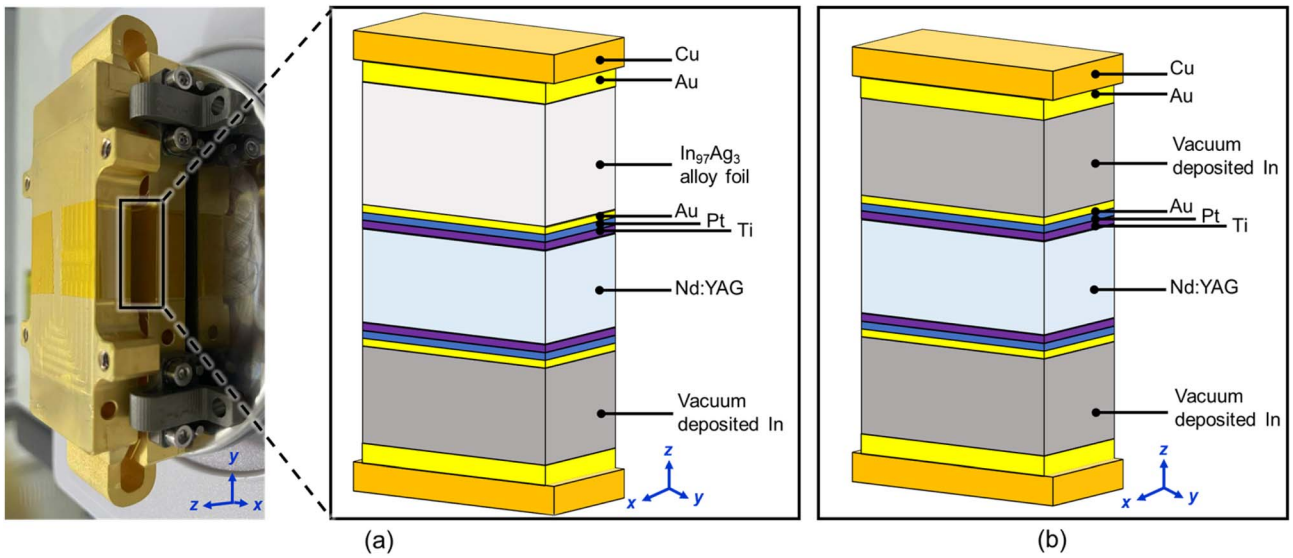

Fig. 1 Schematic of the pre-brazing setup for the (a) experiment group and (b) practical application.

thermal stress limitations of traditional packaging and provides innovative solutions for space applications of high-power lasers.

2.3. Microstructure characterization and performance testing

In order to facilitate subsequent microstructure analysis and improve imaging quality, a sandwich-structured specimen (Cu/YAG/Cu) was obtained from the prepared laser system component into a block shape by wire-electron cutting. To achieve non-destructive visualization of the effective brazing rate at the Cu/YAG weld interface, 3D tomographic imaging of the weld specimen was performed on high-resolution computed tomography (CT) equipment (Xradia 620 Versa, GER). The "large field of view" mode was adopted with a pixel size of 9.94 μm, energy of 21.0 W and exposure time of 1 second. The raw data were processed using the Dragonfly software and quantitatively analyzed on the ImageJ software. Then, the specimens were ground, polished, and cleaned with acetone. The micro morphology of the brazing weld was observed using field emission scanning electron microscopy (FESEM, ZEISS Sigma

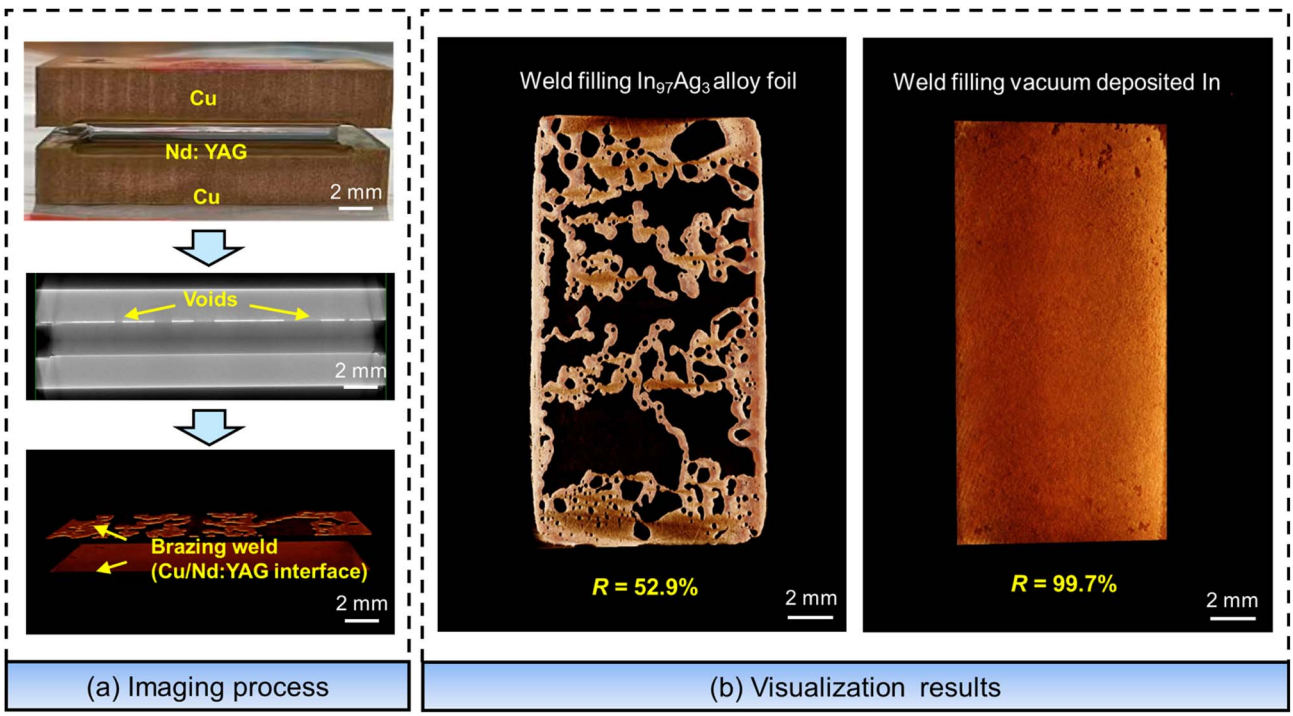

Fig. 2 Effective brazing rate analysis of the Cu/Nd:YAG interface: (a) imaging process and (b) In-F weld and In-D weld visualization results.

500, GE) and elemental mapping was analyzed using energy dispersive spectroscopy (EDS, Oxford Aztec, UK). The original EDS mapping was filtered and processed to improve signal accuracy (such as Pt and Au with similar characteristic X-ray emission energies). To further confirm the type and spatial configuration of the compounds formed within the brazing weld, the weld specimen was precisely excavated and thinned using focused ion beam technology (FIB, Helios 5UX, USA). The obtained foil was analyzed using transmission electron microscopy (TEM, Thermo Scientific Talos F200X, USA). The selected area electron diffraction (SAED) results were processed with reference to the powder diffraction file (PDF) database provided by the international centre for diffraction data (ICDD).

The key concerned properties were tested on the as-welded laser component specimens. To evaluate the interface strength of the Cu/YAG brazing weld, shear tests were performed on a microcomputer-controlled electronic universal material testing machine (DAGA4000, US). The loading rate was set at 0.5 mm min^{-1}.

Considering that the structural thermal stress of a component in operation is difficult to measure directly, the finite element simulation was carried out. It was modeled and calculated using the Structure module of Simcenter Nastran and thermal module of Simcenter 3D Space System, respectively. The reliability of the simulation results was verified by comparing the data collected. A series of optical spot quality experiments were conducted. When the seed light was incident on this Nd laser component and the LD pump light was simultaneously activated, the laser output was triggered. And the spot pattern was captured by the CCD *via* the measured infrared imaging instrument (FOTRIC 240M, CN).

3. Results and discussion

3.1. The effective brazing rate analysis

The effective brazing rate (R, the area ratio of the attached brazing filler metal to the crystal/metal contact interface) could intuitively

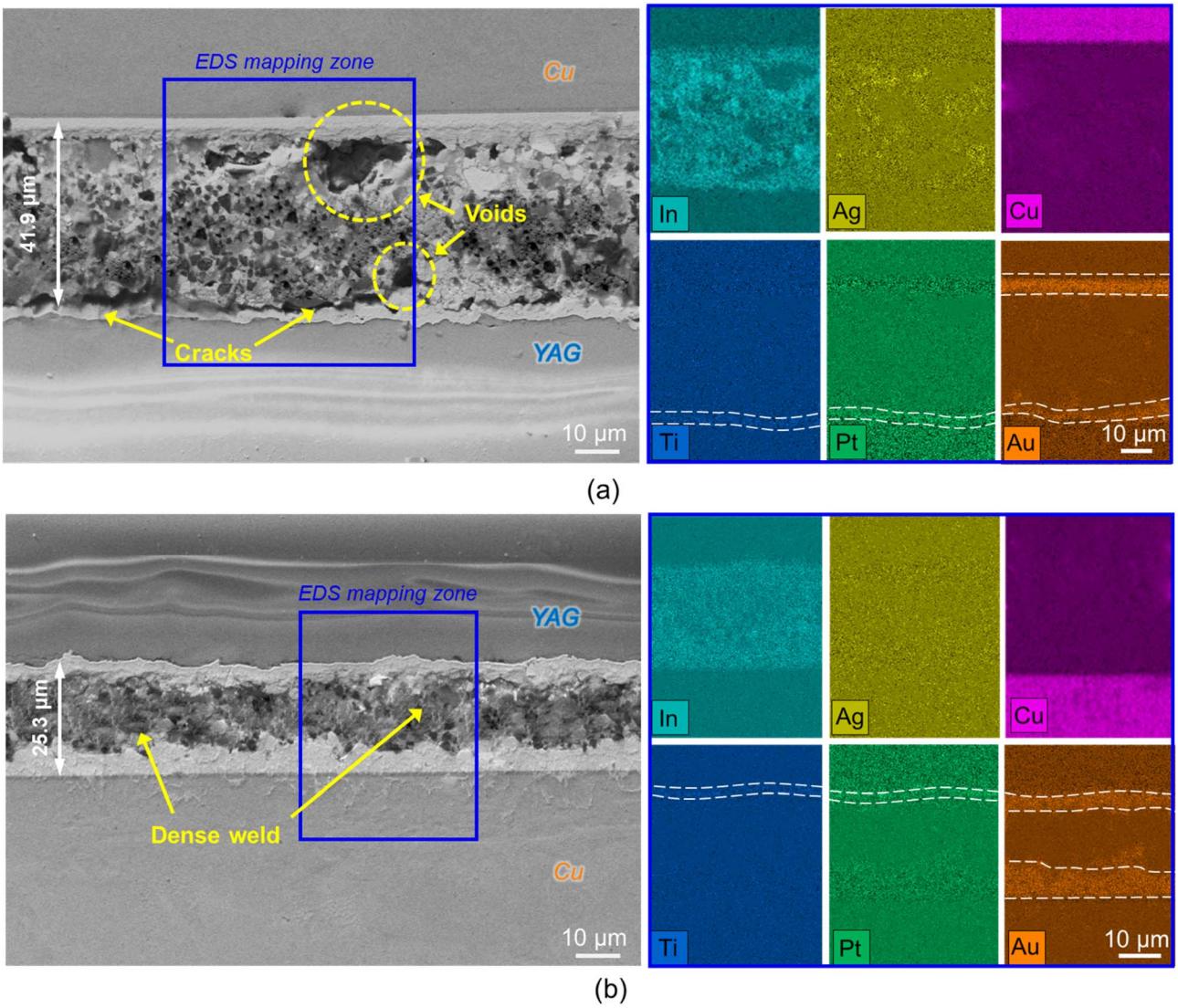

Fig. 3 Weld microstructure analysis including the SEM images with EDS elemental mapping: (a) upper weld filling $In_{97}Ag_3$ alloy foil and (b) lower weld filling vacuum-deposited In.

reflect the brazing quality and the metallurgical behavior of the filler metal, such as wetting and chemical reactions. A higher R is usually expected because it corresponds to higher bonding strength and structural stability. Fig. 2(a) shows the extracting flow of the welding layer, and the high-quality CT imaging results of the Cu/YAG weld interface are depicted in Fig. 2(b). Given that gray-scale differences in CT images are related to the density and thickness of materials, high-density materials have higher radiation absorption rates and higher brightness. Compared with the Cu substrate, the In brazing filler metal has a higher atomic number and density, resulting in bright zones in the CT images. A large number of voids were found on the upper weld filling $In_{97}Ag_3$ foil (In-F), and the bonding effect was poor (R = 52.9%). On the contrary, the lower weld filling vacuum-deposited In (In-D) exhibited a dense brazing weld (R = 99.7%), which facilitated structural stability and performance stability of the studied laser system component in space applications.

3.2. The weld microstructure

Fig. 3 shows weld formation with the EDS mapping of weld filling $In_{97}Ag_3$ foil (In-F) and weld filling vacuum deposited In (In-D). As shown in Fig. 3(a), the thickness of the entire brazing weld was detected at 41.9 μm. The EDS mapping result indicated that the Ti, Pt and Au coating remained intact, as designed for the transition layer, barrier layer, and reaction layer, respectively. Due to the similar expansion coefficient (8.9 $\times$ 10^{-6} K^{-1} at 190 °C for Ti and 6.9 $\times$ 10^{-6} K^{-1} for Nd:YAG), Ti was chosen to regulate thermal stress.[27,28] The Pt line was displayed clearly, indicating that it effectively inhibited In penetrating from the weld into the YAG side. During the fusion process, the element of the $In_{97}Ag_3$ alloy foil diffused into the Au coating on both the Cu- and YAG-sides. It promoted the metallurgical combination and exhibited the white compounds. The intermetallic compound layers enriched with Au and In on the Cu- and YAG-sides were calculated at ~4–5 μm and ~2–3

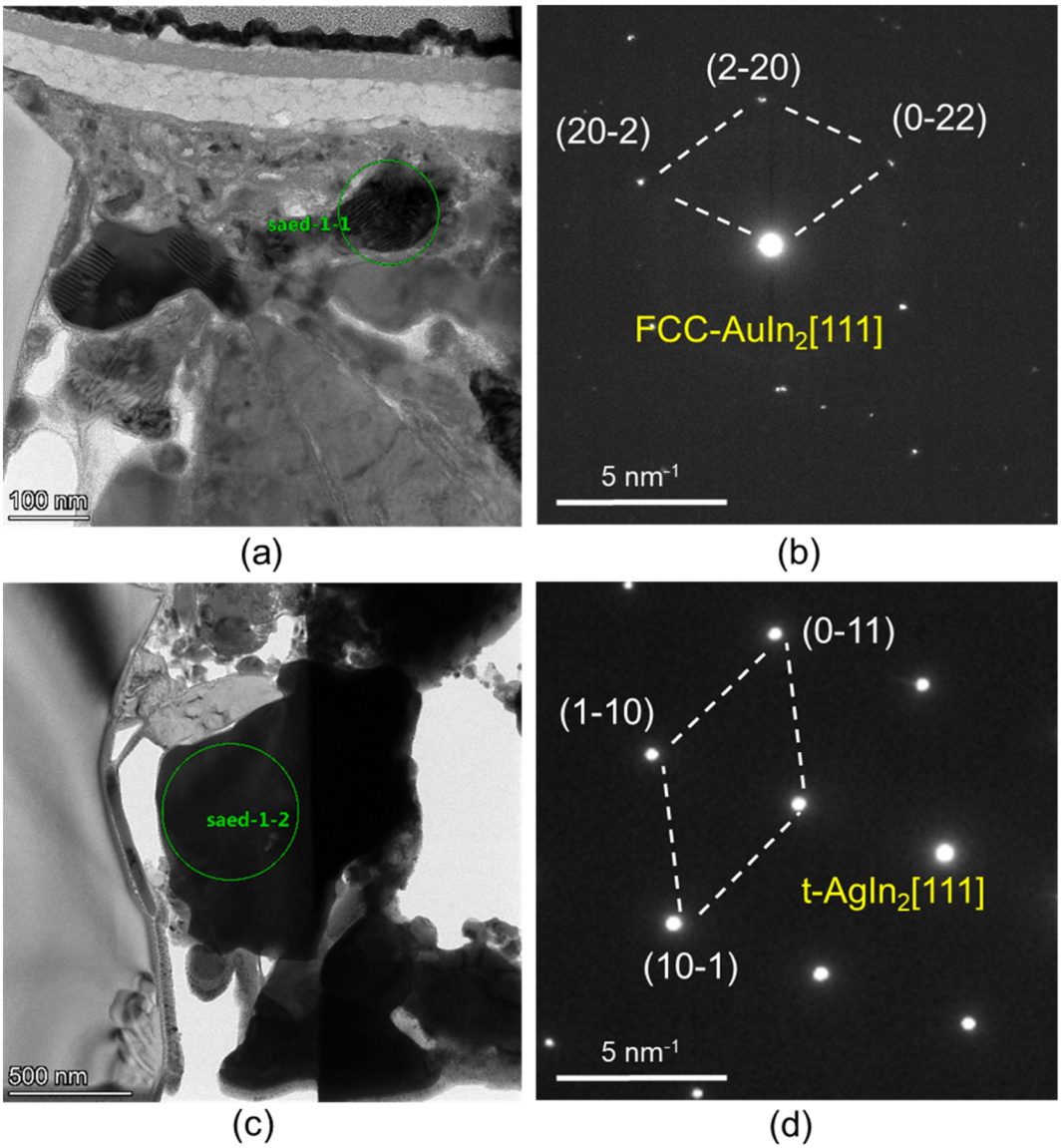

Fig. 4 TEM with SAED analysis of the compounds within the weld filling $In_{97}Ag_3$ alloy foil: (a and b) $AuIn_2$, (c and d) $AgIn_2$.

μm, respectively. Besides, some scattered compounds enriched with Ag and In were found in the brazing weld. However, a large number of voids and cracks existed in the weld, especially near the weld boundary, which worsened performance of the joint.

In comparison, as shown in Fig. 3(b), the lower In-D weld was dense with none obvious defects. The weld was relatively thin with a thickness of 25.3 μm. As displayed in the EDS mapping for the In element, the brazing filler metal was uniformly spread at the Cu/YAG interface. IMC layer thicknesses on the Cu- and YAG-sides were calculated at ~6–8 μm and ~3–5 μm, respectively. A thicker reaction layer indicated a more complete mixing and reaction of elements (Fig. 3(b)).

TEM with SAED analysis was performed on the FIB specimens extracted in the reaction layer for confirming the formed compound type. As shown in Fig. 4 and 5, at 190 °C, the In-F and In-D welds confirmed the FCC-structured $AuIn_2$ formation according to the following reaction: 2 In (l) + Au(s) → Au In 2(s). It was worth noting that $AuIn_2$ compounds were formed at a lower temperature (190 °C) and could withstand higher temperature (200–600 °C), exhibiting good adaptability for the studied laser component for space applications with a large diurnal temperature difference. Simultaneously, Ag in the $In_{97}Ag_3$ alloy foil accelerated the formation of some t-staged $AgIn_2$ particles according to the reaction 2 In (l) + Ag(s) → Ag In 2(s), as shown in Fig. 4(c and d).

3.3. Shear test

Fig. 6 depicts the shear curves of welds filling In solder in different forms. The maximum shear force of the In-F weld was 475 ± 22 N while the maximum of the In-D weld was higher at

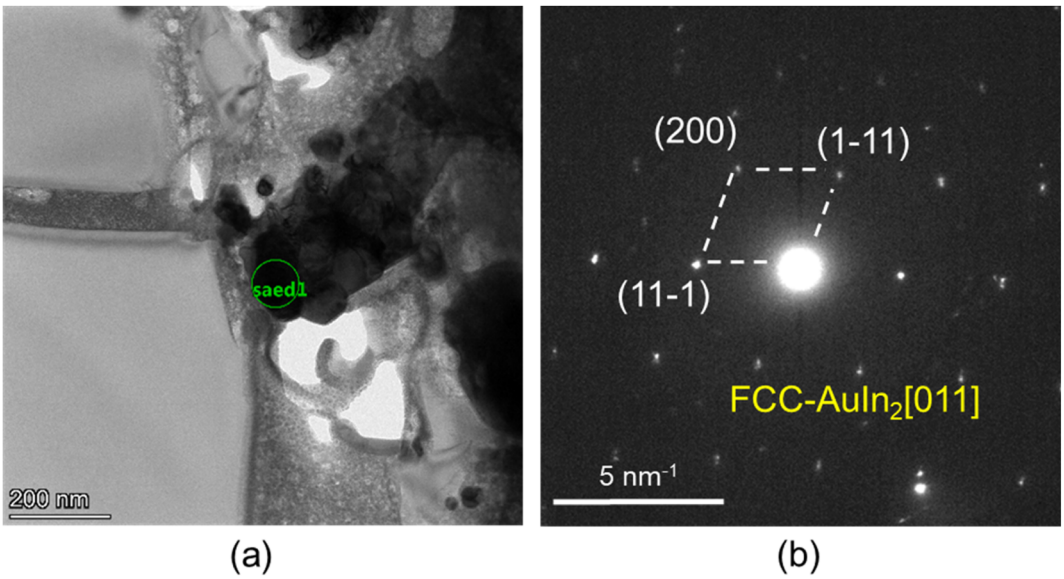

Fig. 5 TEM with SAED analysis of the compounds within the weld filling vacuum-deposited In: (a and b) $AuIn_2$.

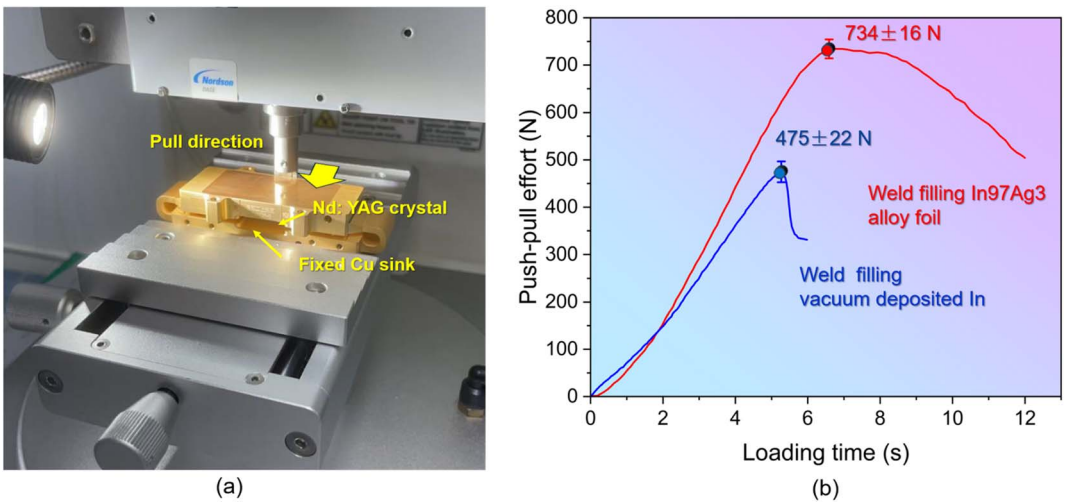

Fig. 6 Shear test analysis: (a) experimental setup and (b) stress–displacement curves of the weld filling $In_{97}Ag_3$ alloy foil and weld filling vacuum-deposited In.

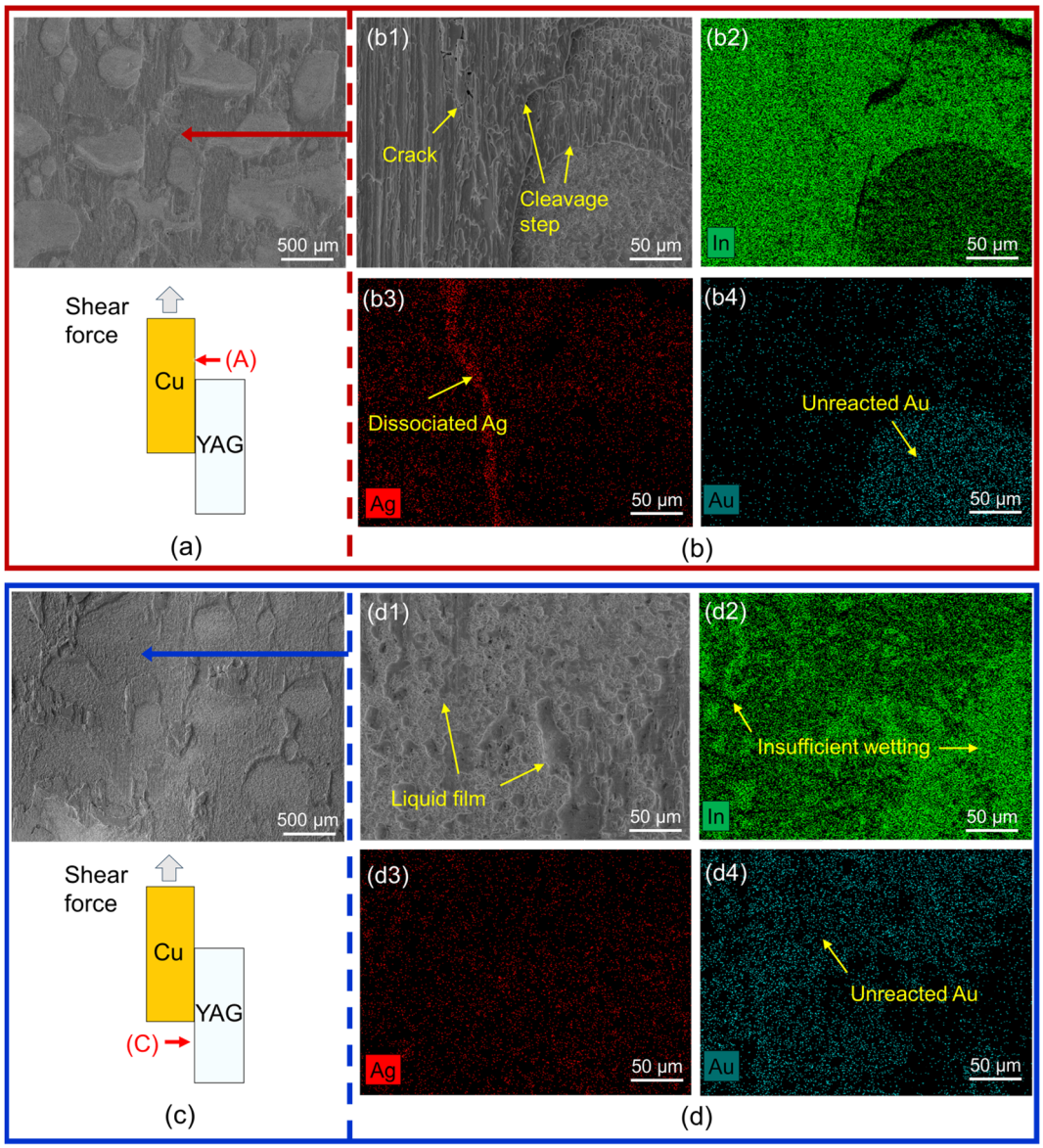

Fig. 7 SEM images with EDS fracture analysis of the weld filling $In_{97}Ag_3$ alloy foil: (a and b) Cu-side surface, (c and d) YAG-side surface.

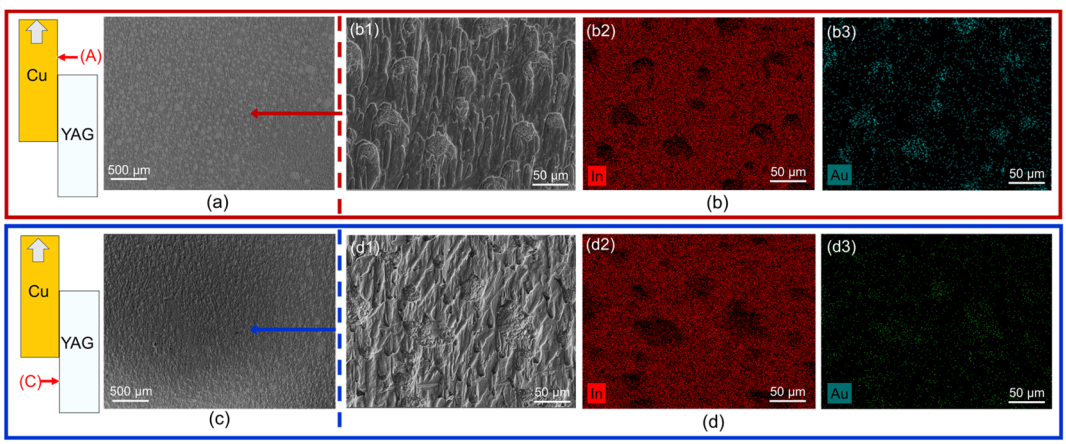

Fig. 8 SEM images with EDS fracture analysis of the weld filling vacuum-deposited In: (a and b) Cu-side surface, (c and d) YAG-side surface.

734 ± 16 N. Fig. 7 displays the fracture morphologies of the In-F weld. As shown in Fig. 7(a), the Cu-side fracture surface exhibited an overall porous morphology. The high-magnification SEM image (Fig. 7b1) revealed distinct cracks and cleavage steps, indicating that brittle fracture occurred at the interface. EDS mappings (Fig. 7b2–b4) demonstrated that large areas of Au remained exposed, suggesting incomplete Au–In interfacial reaction during brazing. In addition, Ag was found locally enriched in the free state (Fig. 7b3), which corresponded to the crack locations in the SEM image. This non-uniform distribution of free Ag was presumed to induce local stress concentrations and promote crack initiation. On the YAG-side fracture surface (Fig. 7(c)), numerous irregular voids were also observed, indicating brittle fracture. The high-magnification SEM image (Fig. 7d1–d4) displays residual filler liquid-film, implying insufficient molten solder spreading. In all, the fracture mode of the In-F weld exhibited a mixed brittle Au/In and ductile In/In failure. As shown in Fig. 8, the dense In-D weld promoted ductile failure with uniform and fine equiaxed dimples.[6,29] In this case, failure primarily occurred within the In/In region of the weld bead.

4. Discussion

4.1. Interface strength analysis

The effect of the solder form on the weld interface strength was analyzed and is illustrated in Fig. 9. For the $In_{97}A_{g3}$ alloy foil, the foil surface is susceptible to oxidation, which hinders subsequent fusion joining and is difficult to remove by manual scraping. In addition, in the In–Ag–Au trimetallic system, the diffusion rate of In is markedly higher than that of Ag and Au (In > Ag > Au). The Kirkendall effect promotes rapid migration of In atoms, resulting in the formation of Kirkendall voids on the weld side of the dissimilar interface. Moreover, free Ag atoms tend to cluster due to diffusion lag, thereby providing additional sites for void initiation. These factors collectively lead to a lower welding efficiency of 52.9% and reduced shear strength. The final joint exhibits a mixed brittle–ductile fracture mode, with cracks initiating and propagating along the In/In and In/Au interfaces.

In contrast, when employing the vacuum-deposited indium layer, the welding surface achieves dense metallurgical bonding with a high welding efficiency of 99.7%. In this case, a thicker $AuIn_2$ layer is formed, indicating a more complete interfacial reaction. The mitigation of the Kirkendall effect may be associated with the reduced overall weld thickness (*i.e.*, shorter diffusion distance), which limits vacancy accumulation and thus suppresses void formation. Ultimately, compared with commercial $In_{97}A_{g3}$ solder foil, the trade-off between strength and void suppression in the thick IMC-layer condition is overcome by adopting vacuum-deposited indium. The optimal joint exhibited a 35.3% improvement in joint strength and a fully ductile fracture mode at the In/In interface.

4.2. Thermal stress simulation

In view of the improved weld quality by filling vacuum-deposited In, practical laser components were prepared with both sides of Nd:YAG using deposited In. In order to evaluate the regulation effect of thermal stress on the prepared

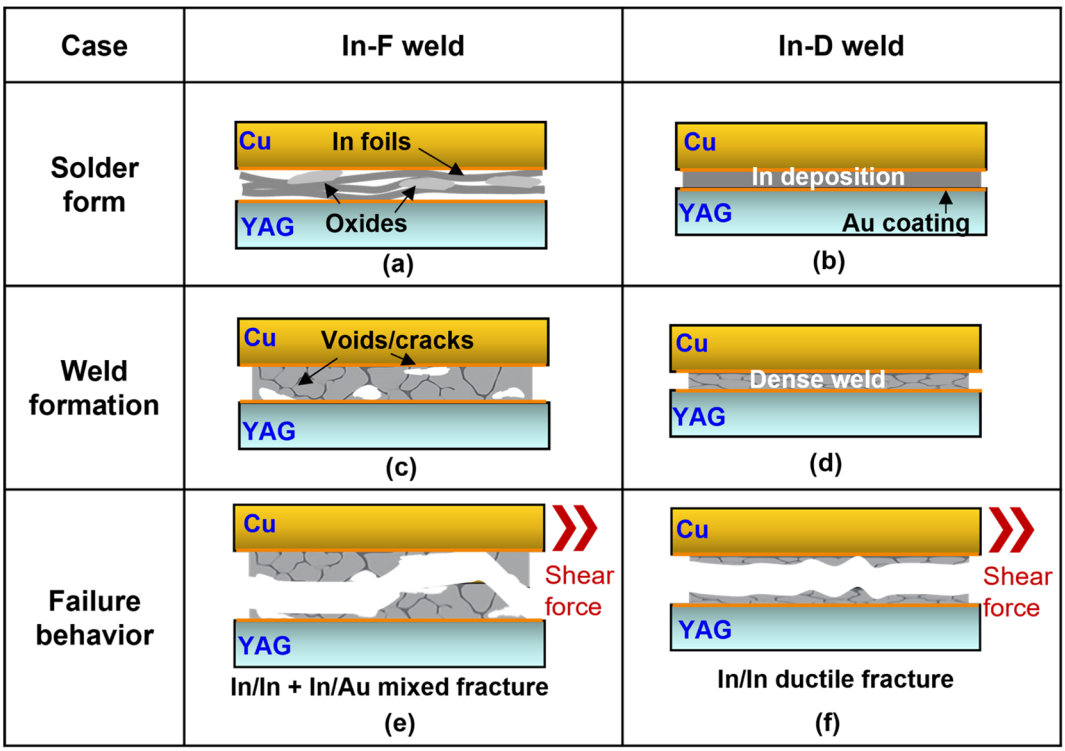

Fig. 9 Schematic of the weld formation and failure behaviour under different solder forms: (a), (c) and (e) In-F weld, (b), (d) and (f) In-D weld.

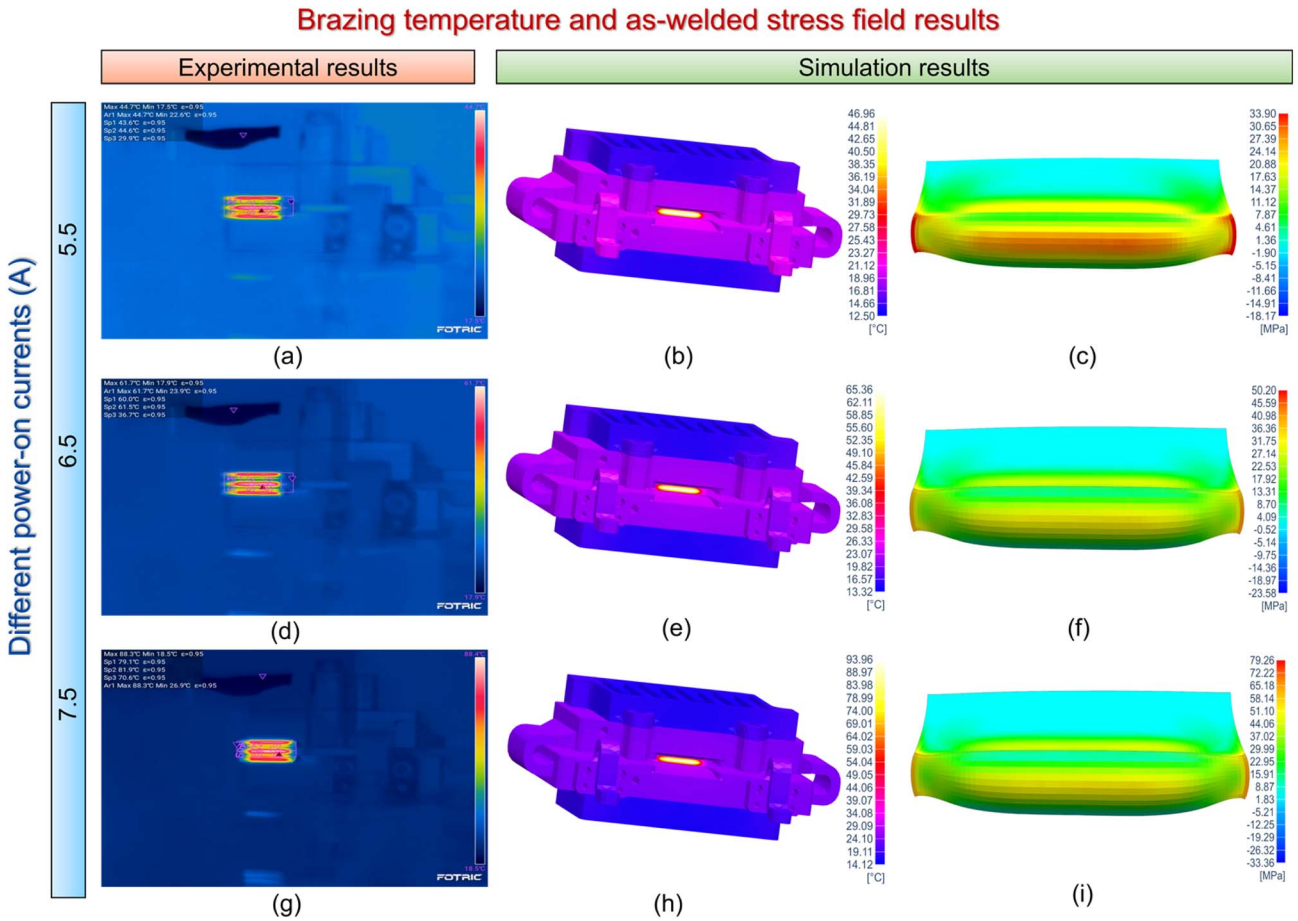

Fig. 10 Thermal stress simulation analysis at 5.5 A, 6.5 A and 7.5 A: (a), (d), and (g) crystal temperature measurement mapping; (b), (e), and (h) crystal temperature simulation mapping; and (c), (f), and (i) crystal thermal stress simulation mapping.

components, simulation tests were conducted at operating currents of 5.5 A, 6.5 A, and 7.5 A.

As shown in Fig. 10(a), (d) and (g), the temperature of Nd:YAG laser components was monitored in real-time. These test conditions were designed to simulate extreme operating scenarios that may be encountered in practical applications, which is critical for assessing the thermal stability of thin-strip Nd:YAG laser crystals. Even at the highest power-on current of 7.5 A, the experimental result shows that the temperature of the thin-strip laser crystal Nd:YAG component remains stable at 88.30 °C ± 2 °C, demonstrating reliable thermal performance under high-power excitation. A pronounced positive correlation was observed between the maximum crystal temperature and the fraction of LD pump power converted into absorbed power.

When the pump current reaches its rated working current of 7.5 A, the simulated temperature rise of the Nd:YAG thin-strip laser crystal is 93.96 °C, which is in agreement with the experimental result. The close consistency between the experimental and simulated temperature fields confirms the accuracy and reliability of the established thermal model (Fig. 10b, e, and h). Based on this, subsequent thermal stresses were calculated through thermal-mechanical coupling.

Fig. 10(c), (f) and (i) provide thermal stress calculation results of power-on laser components. It is clearly observed that the maximum principal stress mainly occurs in the central region of the Nd:YAG crystal after welding. This stress localization is primarily associated with welding-induced residual stress and the mismatch in thermal expansion behavior between the Nd:YAG crystal and the Cu substrate. Specifically, residual stress in the welded structure primarily originates from the non-uniform thermal expansion and contraction induced by the highly heterogeneous temperature field during welding, under the constraint of both ends of the crystal (shown in red). During practical operation, the difference in thermal expansion coefficients between Nd:YAG and Cu further intensifies stress accumulation during repeated heating and cooling cycles, thereby contributing to the observed stress concentration in the central region. When the maximum absorbed power reaches

Table 1 Thermal cycle test conditions

Condition	Value
Pressure (atm)	1
Maximum temperature (°C)	+40
Minimum temperature (°C)	−10
Cycle times	12.5
Rate of temperature change (°C min^{-1})	5
Storage time (h)	2

Table 2 Mechanical vibration test conditions

Condition	Value
Frequency range (Hz)	10–80; 80–350; and 350–2000
Power spectral density ($dB\ oct^{-1}$; $g^2\ Hz^{-1}$; and $dB\ oct^{-1}$)	+3; 0.04; and −3
Total root mean square value	6
Loading direction	*X*, *Y*, and *Z*
Test duration (min) in each direction	5

200.4 W at 7.5 A, the maximum principal stress value is 79.26 MPa, as shown in Fig. 10(i), far below the fracture threshold of 206 MPa.[30] It indicates that the crystal structure has a relatively high safety margin and verifies industrial feasibility of the proposed low-temperature brazing welding process. Chen *et al.*[31] reported that the crystal temperature of Nd:YAG and other laser crystal devices increased to 638.43 K under an operating pump power of 80 W. In contrast, the Nd:YAG laser crystal brazed-sealing structure developed in this work exhibits a much lower steady-state temperature of 361.45 K experimentally and 367.11 K numerically, even under a significantly higher service power of approximately 576 W.

4.3. Laser spot quality evaluation

To verify the industrial applicability of the welded structural components in extreme space environments, the laser spot quality was evaluated. Considering the severe diurnal temperature variation and navigating satellite vibration, the study simulated this service condition through thermal cycling tests (Table 1) and multi-axis vibration dynamic tests (Table 2). For laser components with In-D and In-F welds, static testing (without pump light) and dynamic testing (with pump operating currents of 5.5 A, 6.5 A, and 7.5 A) for spot morphology were conducted on the initial welded samples and heated/oscillated samples. It is worth noting that the testing also incorporates comprehensive testing and characterization with fast power-on startup power supply and fast power-off shutdown power supply. As shown in Fig. 11, all tested Nd:YAG-based laser components with In-F and In-D welds exhibited

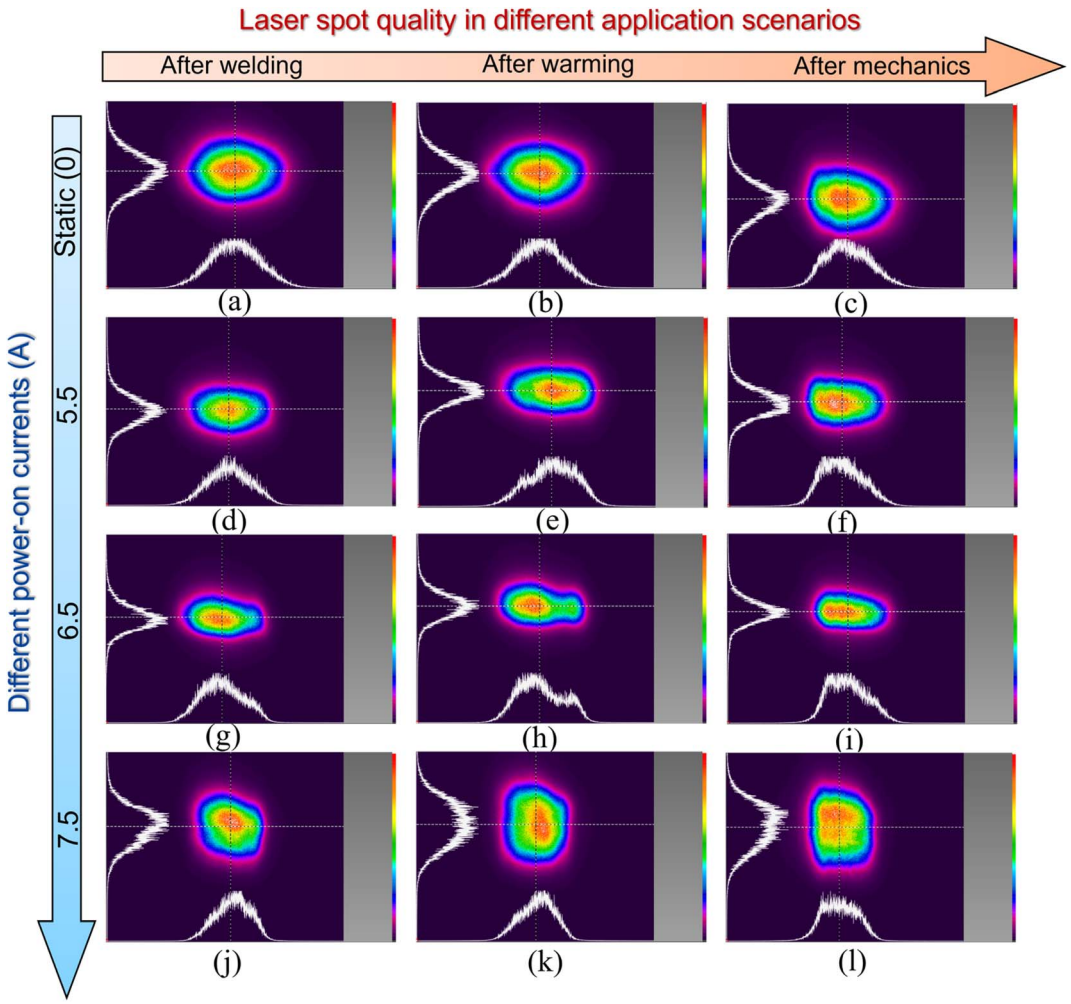

Fig. 11 Comparison of the spot morphologies of Nd:YAG-based laser components with In-F and In-D welds. Spot shapes after welding, temperature cycling, and mechanical vibration in: (a–c) static condition and dynamic conditions with power-on currents of (d–f) 5.5 A, (g–i) 6.5 A, and (j–l) 7.5 A.

"fluctuating" spot morphologies. The beam profiles deviate from ideal elliptical shapes, displaying tailing, double peaks, and degraded focusing performance. The spot diameters are relatively large, accompanied by increased divergence angles, and wavefront integrity is further compromised by aberrations introduced during free-space propagation. In addition, the center-of-mass coordinates of the spot show significant displacement in the X/Y directions, which can be attributed to mechanical vibration and airflow disturbances. The occurrence of multiple intensity peaks or saddle-shaped distributions arises from interference-induced intensity fluctuations, leading to degradation of the beam quality factor (M^2).

These results demonstrate that excessive porosity associated with the In-D/In-F welding schemes can induce system instability, trigger cascading amplification of welding defects, deteriorate heat-dissipation capability, and promote local stress concentration during operation.

The double-sided indium coating (In-D/In-D) configuration was adopted as the optimized group. After a series of laser-quality tests, it was confirmed that the components exhibited no cracking. Fig. 12 shows the static laser spot of the component under power-off conditions, as well as the dynamic spot profiles at different operating currents of 5.5 A, 6.5 A, and 7.5 A. Regardless of the power state, the emitted laser spots were tightly Gaussian focused and symmetric, with no observable trailing or distortion, *i.e.*, the center of mass offset was small. That is to say, in the In-D/In-D welding scheme testing, due to low optical path loss and scattering, good wavefront integrity, weak mechanical vibration and airflow disturbance, and insignificant interference effects, the total energy is stable and close to the theoretical value, the diameter is close to the diffraction limit, the center of mass offset is small, and the peak intensity shows a single peak Gaussian distribution.

To further quantify the improvement in laser spot quality, the spot circularity was evaluated using the ImageJ software, defined as circularity $= 4\pi S\, C^{-2}$, where S is the spot area and C is the spot perimeter. A circularity closer to 1 indicates a shape approaching an ideal circle. As shown in Fig. 13, the optimized laser spots exhibit circularity generally higher than 0.90, and consistently exceed those of the unoptimized samples under the

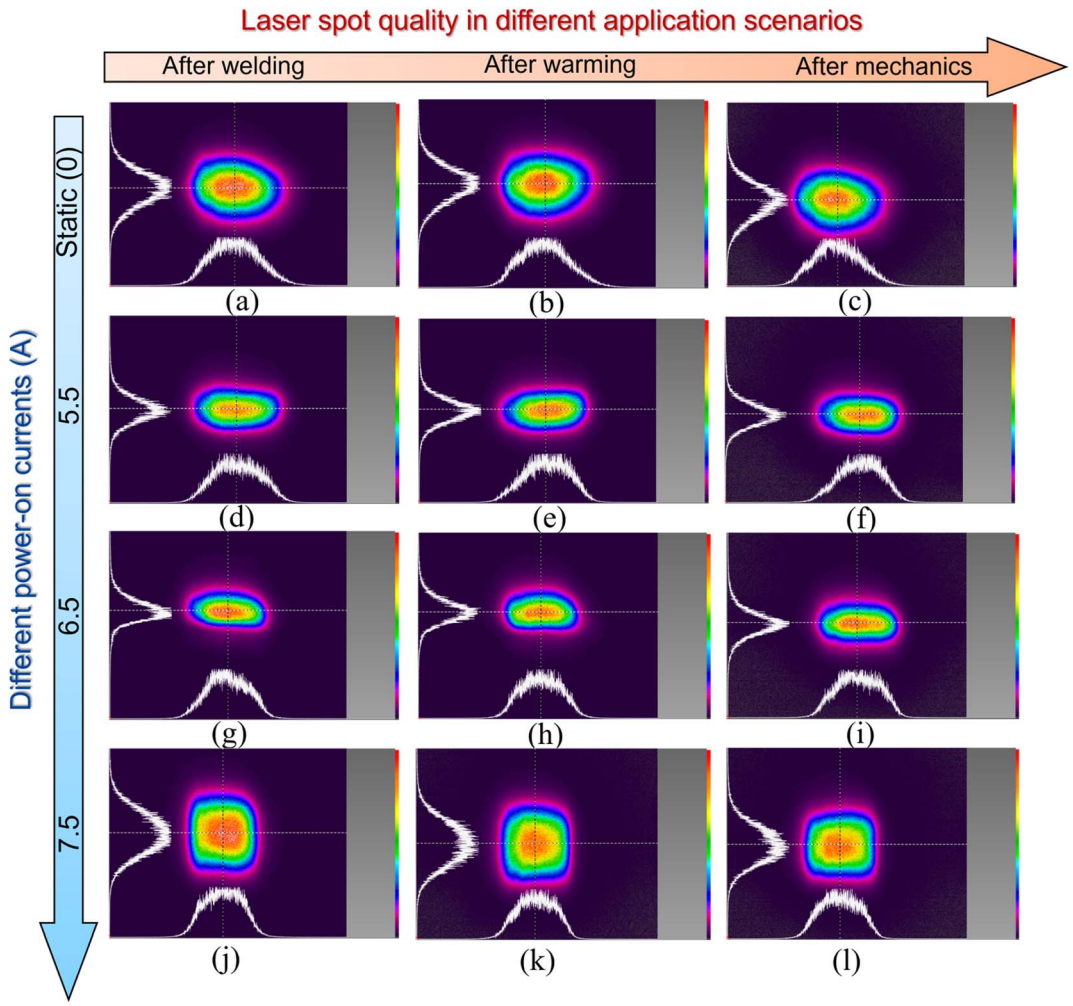

Fig. 12 Comparison of the spot morphologies of Nd:YAG-based laser components with In-D and In-D welds. Spot shapes after welding, temperature cycling, and mechanical vibration in: (a–c) static conditions and dynamic conditions with power-on currents of: (d–f) 5.5 A, (g–i) 6.5 A, and (j–l) 7.5 A.

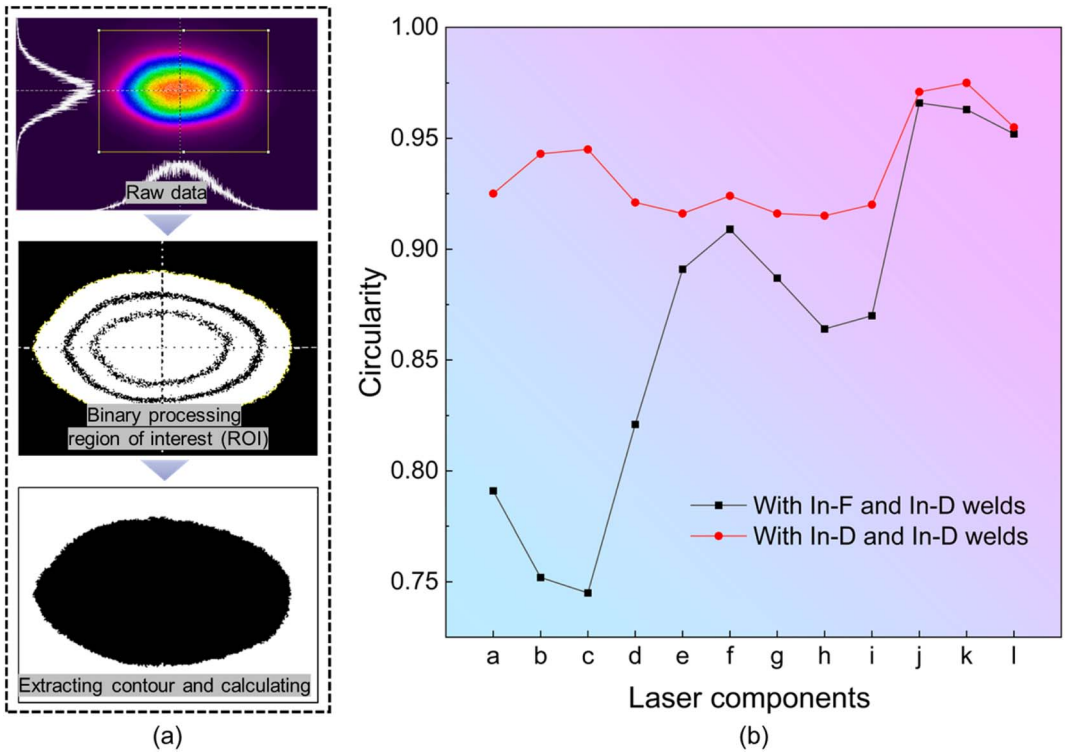

Fig. 13 Quantitative evaluation of beam quality: (a) process flow and (b) statistical results.

same operating conditions. It demonstrates that the proposed optimization strategy significantly improves beam symmetry and focusing quality.

The reasons for the fluctuation of the laser spot in laser components with In-D and In-F welds could be concluded as: (1) thermal conduction imbalance: dense voids on the upper welding surface significantly reduce the thermal conductivity, hinder the transfer of heat to the heat sink and form a local high-temperature zone. Also, the lower welding surface has no voids to achieve efficient heat dissipation. This asymmetric thermal distribution leads to uneven refractive index gradients within the crystal, resulting in wavefront distortion when the beam passes through. (2) Asymmetric mechanical support: cavities weaken the stability of the rigid connection on the upper welding surface, resulting in micro-nano level displacement under temperature cycling or mechanical vibration; the dense structure of the lower welding surface maintains firm support. This unilateral constraint results in a slight tilt of the Nd:YAG optical axis of the crystal, amplifying the position shift and deformation of the emitted light spot. (3) Residual stress concentration: a stress concentration zone is formed around the cavity, and laser-induced microcracks propagate inside the Nd:YAG crystal, further disrupting optical uniformity. While matching the coefficient of thermal expansion (CTE) effectively controls macroscopic deformation, localized microscopic defects can generate high-frequency spot fluctuations through thermal-mechanical coupling. This occurs *via* a sequential process, in which localized temperature elevation initiates thermal stress accumulation, which subsequently causes micro-scale structural deformation, ultimately leading to optical path segregation or disruption.

It is concluded that In-F/In-D welds in the laser system preparation process, the large void defect should be prevented in the welded structure, which destroys the beam quality consistency through asymmetric heat conduction and mechanical instability. In other words, this triple coupling mechanism of "structural defects-thermodynamic imbalance-optical distortion" will ultimately manifest as an increase in total energy loss, deterioration of wavefront RMS error, and loss of positioning accuracy due to the rise of beam quality factor M^2, which will affect the quality of the light spot. The symmetric and well-rounded laser spot observed in In-D/In-D welded components arises from enhanced metallurgical bonding facilitated by symmetrical heat distribution and improved mechanical stability at the dissimilar interfaces.

5. Conclusions

This study systematically investigated the potential of a low-temperature brazing welding process in achieving low thermal stress and high-strength interface of Nd:YAG-based advanced laser components. The findings were concluded as follows:

(1) Reliable joints between Cu and Nd:YAG were successfully achieved at a low temperature of 190 °C. In contrast to the weld with a relatively low effective brazing rate of 52.9% filling conventional $In_{97}Ag_3$ alloy foil, the one using vacuum-deposited In filler significantly improved the weld filling ratio to 99.7%, resulting in a dense welding layer and effective metallurgical bonding.

(2) A high-strength Cu/Nd:YAG interface was obtained. The optimal joint by adopting vacuum-deposited In as the welding

layer exhibited a 35.3% improvement in interface strength compared with one filling $In_{97}Ag_3$ alloy foil. The fracture surface displayed ductile shear failure within the In solder zone.

(3) Finite element simulations were employed to visualize the thermal stress conditions. Under maximum operating current of 7.5 A, the optimized laser component still sustained a principal stress of 79.26 MPa, which remained far below the fracture threshold of Nd:YAG (206 MPa), verifying its structural safety and possessing the reliability of space applications.

(4) The laser beam spot quality of the manufactured laser component was evaluated under actual space application conditions. Void defects can induce thermodynamic instability at the dissimilar interface, thereby leading to spot distortion. By adopting the optimized vacuum-deposited indium coating as filler, the resulting laser component exhibited space-grade beam quality, characterized by a tightly focused and highly-concentrated-energy laser spot.

Author contributions

Baolin Zhang: experiment and characterization, methodology, investigation, experimental data and images organization, and writing–original draft. Xiaojian Xu: characterization, investigation, experimental data and images organization, and writing–original draft. Guangwei Sun: experimental design, test characterization, technical guidance, and project administration. Cheng Yang: experiment simulation and experimental guidelines. Wenhui Yang: Welding experiment. Ge Zhang: TEM characterization. Pan Feng: crystal metallization experiment. Jiangyun Miao: experiment on indium evaporation. Haichao Cui: experimental plan guidance and paper Revision. Mingjian Wang: project administration, experimental assistance, and paper revision. Guofeng Xin: guidance for experimental work. Xia Hou: platform support and department management. Weibiao Chen: funding acquisition and project chief manager.

Conflicts of interest

The authors declare that they have no known competing financial interests or personal relationships that could have appeared to influence the work reported in this paper.

Data availability

Data will be made available upon reasonable request.

Acknowledgements

This work is supported by the National Key Research and Development Program (2020YFC2200300).

References

1 J. Guo, W. Zhang, Z. Liao, C. Zhang, Y. Yu and X. Zhang, *Photonics Res.*, 2025, **13**, 889–896.
2 G. Huang and W. Xu, *Remote Sens.*, 2024, **16**, 23.
3 N. Suratun, Z. Tukiran, S. Lau Wei, S. N. Rohim, T. Vincent Sia Ing, N. L. Razali and M. Morsin, *J. Electron. Voltage Appl.*, 2021, **2**, 38–48.
4 V. Hariton, C. P. João, H. Pires, M. Galletti and G. Figueira, *High Power Laser Sci. Eng.*, 2020, **8**, e13.
5 J. Liu, Y. Wen, S. Li, L. Gong, C. Wu, Y. Yu, C. Wang and G. Jin, *Opt. Commun.*, 2021, **480**, 126452.
6 H. R. Yang, C. Li, X. Q. Si, J. L. Qi and J. Cao, *Mater. Charact.*, 2024, **211**, 113867.
7 J. Zuo and X. Lin, *Laser Photonics Rev.*, 2022, **16**, 2100741.
8 V. Rastogi and S. Chaurasia, *Photonics*, 2024, **11**, 11100942.
9 K. M. Shu and G. C. Tu, *Mater. Sci. Eng. A.*, 2003, **349**, 236–247.
10 J. W. Yang, C. H. Xie, J. Zhang and J. Qiao, *Mater. Today Commun.*, 2025, **42**, 111502.
11 C. Li, X. Si, J. Cao, J. Qi, Z. Dong and J. Feng, *J. Mater. Sci. Technol.*, 2019, **35**, 2470–2476.
12 C. Li, X. Q. Si, L. Chen, J. L. Qi, Z. G. Liu, Y. X. Huang, Z. B. Dong, J. C. Feng and J. Cao, *Ceram. Int.*, 2019, **45**, 3284–3289.
13 Y. F. Wang, M. Q. Liu, H. Zhang, Z. R. Wen, M. C. Chang, G. J. Feng and D. A. Deng, *J. Eur. Ceram. Soc.*, 2021, **41**, 4273–4283.
14 B. Chen, W. J. Zou, W. W. Li, S. B. Wu, H. P. Xiong and X. Wu, *J. Mater. Sci. Technol.*, 2020, **50**, 13–20.
15 Z. Zhang, J. Li, K. Liu, J. Wang, S. Jian, C. Xu, H. Wang, L. Wang, X. Zhu, A. Okulov, Y. Wei and Y. Yang, *J. Mater. Res. Technol.*, 2023, **26**, 395–416.
16 X. F. Zhang, P. P. Lin, J. C. Lin, W. Q. Zhao, X. Y. Li, J. Yang, C. Wang, T. S. Lin, P. He and Y. L. Zhuang, *J. Mater. Process. Technol.*, 2023, **322**, 118194.
17 S. K. Chaluvadi, S. P. Chalil, F. Mazzola, S. Dolabella, P. Rajak, M. Ferrara, R. Ciancio, J. Fujii, G. Panaccione, G. Rossi and P. Orgiani, *Sci. Rep.*, 2023, **13**, 3882.
18 L. Deillon, T. Hessler, A. Hessler-Wyser and M. Rappaz, *Acta Mater.*, 2014, **79**, 258–267.
19 J. Lian, S. J. W. Chun, M. S. Goorsky and J. L. Wang, *J. Mater. Sci.*, 2009, **44**, 6155–6161.
20 H. K. Sung, C. Wang and N. Y. Kim, *J. Manuf. Syst.*, 2015, **25**, 127002.
21 J. M. Koo and S. B. Jung, *J. Electron. Mater.*, 2005, **34**, 1565–1572.
22 M. Y. Xiong, H. H. Su, B. Zhao, L. Sun, Y. C. Fu, W. F. Ding, J. H. Xu, Z. H. Zhu and F. Pu, *Vacuum*, 2023, **210**, 111905.
23 J. Wen, G. L. Sun, J. Y. Su, Y. Fan, L. Z. Fu, Z. Chen and W. H. Zhu, *J. Mater. Res. Technol.*, 2025, **35**, 1072–1089.
24 J. R. Pérez-Higareda, J. A. Torres, C. Leyva-Porras, O. O. Solís-Canto, C. Torres-Torres, A. Oliver and D. Torres-Torres, *Int. J. Appl. Glass Sci.*, 2025, **16**, e70002.
25 X. R. Meng, X. W. Luo, J. Z. Ye, X. M. Chen, X. G. Zhang, L. Zhang, Q. S. Gao and B. L. Lu, *Photonics*, 2023, **10**, 730.
26 X. R. Meng, X. G. Zhang, X. M. Chen, X. W. Luo, J. Z. Ye, L. Zhang, Q. S. Gao and B. L. Lu, *Opt. Express*, 2023, **31**, 19126–19132.
27 S. Maltsev, O. Dymshits, I. Alekseeva, A. Volokitina, M. Tenevich, A. Bachina, K. Bogdanov, S. Zapalova, G. Shakhgildyan and A. Zhilin, *Materials*, 2025, **18**, 785.

28 K. Pooja, N. Tarannum and P. Chaudhary, *Discov. Mater.*, 2025, **5**, 35.
29 P. P. Lin, T. S. Lin, P. He, M. C. Wang and J. Yang, *Ceram. Int.*, 2019, **45**, 11195–11203.
30 K. S. Shibib, M. A. Minshid and N. E. Alattar, *Therm. Sci.*, 2011, **15**, 399–407.
31 Z. Chen, F. Li, W. Liu, Y. Zhang and Q. Zhang, *Results Opt.*, 2025, **21**, 100899.